Velocity Dependence of Moiré Friction

Yiming Song,[†,1] Xiang Gao,[†,2] Antoine Hinaut,[1] Sebastian Scherb,[1] Shuyu Huang,[1,3] Thilo Glatzel,[1] Oded Hod,[*,2] Michael Urbakh,[*,2] Ernst Meyer[*,1]

[1]Department of Physics, University of Basel, Basel 4056, Switzerland.

[2]Department of Physical Chemistry, School of Chemistry, The Raymond and Beverly Sackler Faculty of Exact Sciences and The Sackler Center for Computational Molecular and Materials Science, Tel Aviv University, Tel Aviv 6997801, Israel.

[3]Key Laboratory for Design and Manufacture of Micro-Nano Biomedical Instruments, School of Mechanical Engineering, Southeast University, Nanjing 211189, China.

Abstract

Friction force microscopy experiments on moiré superstructures of graphene-coated platinum surfaces demonstrate that in addition to atomic stick-slip dynamics, a new dominant energy dissipation route emerges. The underlying mechanism, revealed by atomistic molecular dynamics simulations, is related to moiré ridge elastic deformations and subsequent relaxation due to the action of the pushing tip. The measured frictional velocity dependence displays two distinct regimes: (i) at low velocities, the friction force is small and nearly constant; and (ii) above some threshold, friction increases logarithmically with velocity. The threshold velocity, separating the two frictional regimes, decreases with increasing normal load and moiré superstructure period. Based on the measurements and simulation results a phenomenological model is derived, allowing to calculate friction under a wide range of room temperature experimental conditions (sliding velocities of 1-10^4 nm/s and a broad range of normal loads), and provides excellent agreement with experimental observations.

*Corresponding authors: Michael Urbakh, Oded Hod, Ernst Meyer
Email: urbakh@tauex.tau.ac.il, odedhod@tauex.tau.ac.il, ernst.meyer@unibas.ch
†These authors contribute equally.

Frictional response to shear velocity is of critical importance for energy dissipation and dynamic stability in many mechanical systems.[1,2] This fundamental problem is commonly complicated by distinct physical mechanisms that dominate at various characteristic length scales. For instance, in contrast to Coulomb's law, stating that kinetic friction is weakly dependent on the sliding velocity at the macroscale, at the atomic scale friction often presents logarithmic dependence on sliding velocity, due to thermally activated hopping over atomic potential barriers.[3-7] A more complex behavior can be encountered at the nanoscale, where collective dynamics, e.g. elastic dislocations,[8-10] grain boundaries,[11,12] and moiré superstructures,[13,14] emerge and lead to remarkable energy dissipation that may impact frictional velocity and load dependence. To rationalize frictional characteristics of systems across length scales, it is therefore crucial to unravel the mechanisms underlying such collective effects.

Among these effects, the frictional characteristics of moiré superstructures involving two-dimensional (2D) layered materials, e.g. graphene and molybdenum disulfide (MoS_2), which exhibit superior superlubric properties, became a particular focus of the nanotribology community in recent years.[2,15-19] To achieve superlubricity, surface coating or stacking of 2D materials to form heterostructures are common practices.[20-23] At such junctions, moiré superstructures naturally form due to lattice mismatch and/or misorientation of the contacting surfaces. In practice, the dimensions of these superstructures can be tuned via the material identity and the interfacial twist angle from atomic lattice dimensions up to a few tens of nanometers. The presence of moiré superstructure introduces considerable distortion to the otherwise uniform and planar interfacing lattices, leading to the formation of flat domains of nearly optimal stacking separated by corrugated moiré ridges, where tensile and compressive strain accumulate.[14,24] Previous studies have demonstrated a variety of unique frictional characteristics related to moiré superstructures, including long-range smooth lateral force modulation,[25-27] moiré scale stick-slip dynamics,[28-30] negative friction coefficients,[31] and moiré scattering at grain boundaries.[32] The mechanism underlying many of these phenomena involves the accumulation and sudden release of in- and out-of-plane strain of the corrugated layer during sliding.[13,29-32] This, in turn, suggests the emergence of unique frictional velocity dependence that may have substantial impact on the tribological characteristics of layered material interfaces, which remains to be explored.

To that end, we performed friction force microscopy (FFM) measurement of the frictional velocity dependence of a sharp tip sliding over the moiré superstructures formed between graphene (Gr) and a Pt(111) surface (see Figure 1a). Due to the intrinsic lattice mismatch between the Pt(111) monocrystalline surface and the hexagonal graphene lattice, corrugated moiré superlattice structures are observed with different periodicities of $0.5 - 2.2$ nm depending on the relative twist angle. The out-of-plane corrugation is correlated with the moiré period, varying from a nearly flat to a ~0.3-0.4 Å corrugated surface as the moiré supercell dimension increases.
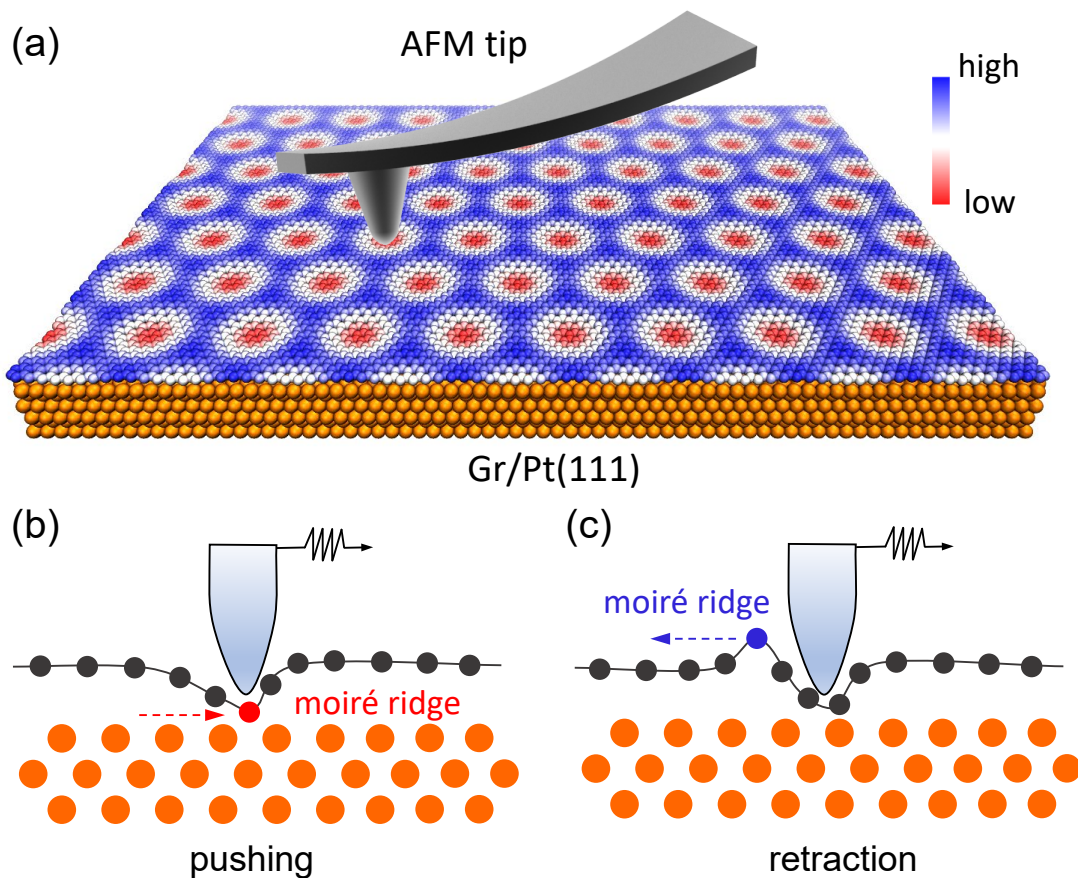
Figure 1. Schematic of the experimental setup and energy dissipation mechanism. (a) Illustration of the AFM tip (out-of-scale) sliding atop a corrugated graphene surface modulated by moiré superlattice structures formed due to its interaction with the underlying lattice mismatched Pt(111) surface (orange). The out-of-plane topography of the moiré superstructure is depicted by the color scheme. (b)-(c) Schematic of the phenomenological model considering strain/stress accumulation (stick) when the AFM tip pushes down and sideways on a moiré ridge (b) and lattice relaxation (c) following strain/stress release (slip).

In our experiments, the tip is dragged in contact mode at a velocity of $1 - 10^4$ nm/s over the corrugated surfaces of three typical moiré superstructures of dimensions 2×2, 4×4 and $\sqrt{67} \times \sqrt{67}$ in units of the graphene lattice constant of 0.246 nm (see Figure 2a-c).[33] The periodicities of the three superstructures are determined via fast Fourier transform (FFT) of the lateral force maps to be ~0.5, ~1.0 and ~2.1 nm, respectively (see Figure 2d-f). Both the graphene atomic lattice and the moiré superlattice are clearly resolved in the topography maps (Figure 2a-c) and the corresponding lateral force maps (Figure 2d-f). This confirms the atomic cleanness, purity, and high-quality of the graphene prepared and measured under UHV conditions. During the friction force measurements, unless otherwise noted, the normal load was kept constant at a value of $F_N = 2$ nN, where the reference zero load is defined at the point where the cantilever does not bend. Further details regarding the experimental setup are provided in Supplementary Information (SI) sections 1-3.
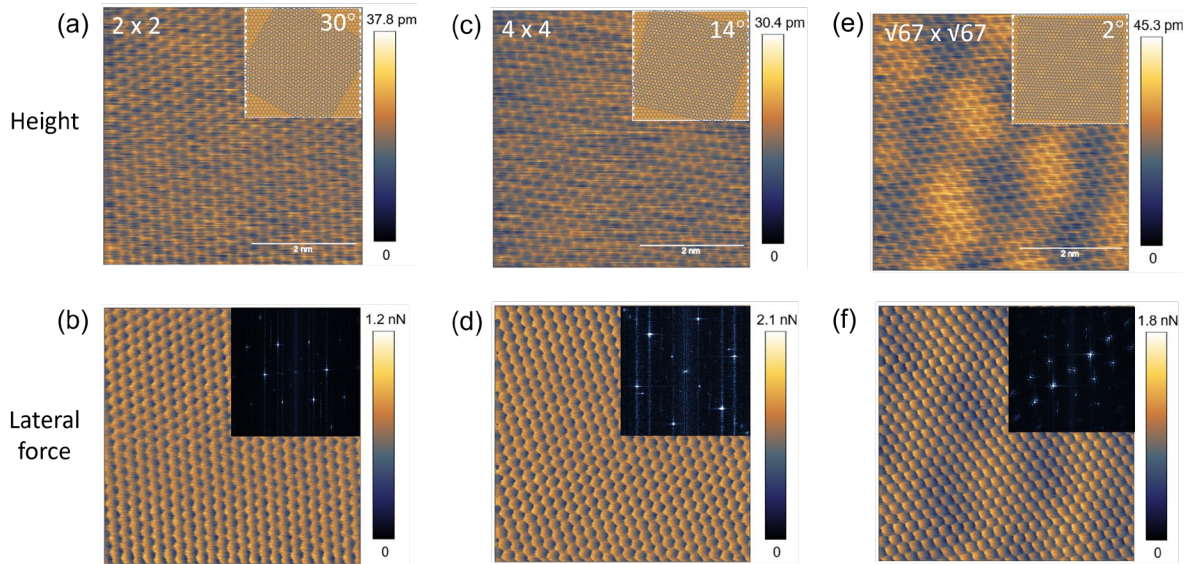

Figure 2. Topography and lateral force measurements of the moiré superlattice formed at a graphene layer deposited on a Pt(111) surface. (a-c) Height images of 3 different moiré patterns over a scan area of 5×5 nm^2 (the insets show schematic illustrations of the relative orientation between graphene and Pt(111) surface at the corresponding twist angles) and (d-f) the corresponding lateral force maps (insets show the FFT analysis). Due to the cross talk between the bending and torsion modes of the cantilever, the topographies in panels a-c provide only a rough estimation of the actual moiré superstructure corrugation.

Figure 3a shows a typical velocity dependence of the mean friction force atop the $\sqrt{67} \times \sqrt{67}$ moiré pattern, rendering two distinct regimes: (i) at low velocities $(1 - 100 \, \text{nm/s})$, a nearly constant ultralow friction force $(\sim 0.01 \, \text{nN})$ is measured, which is comparable to the value measured for pristine graphene grown under UHV on silicon carbide;[16] (ii) at higher velocities, friction increases logarithmically with velocity demonstrating a fourfold enhancement (up to $\sim 0.04 \, \text{nN}$) when the velocity is increased by two decades (from 10^2 to $10^4 \, \text{nm/s}$).

To reveal the origin of these two frictional regimes, we compare in Figure 3b-c maps of the average lateral force (half the difference between the lateral forces measured at each location during forward and backward scanning, respectively) obtained at a lower $(4.1 \, \text{nm/s})$ and a higher $(390.6 \, \text{nm/s})$ sliding velocity. Both maps clearly manifest atomic scale features with periodicity that corresponds to the hexagonal graphene lattice along the sliding direction. Notably, on top of the atomic features, the higher velocity map shows also larger-scale higher-friction patterns with periodicity that matches that of the moiré lattice. This indicates that the appearance of a new energy dissipation mechanism at high sliding velocities originates from the corrugated moiré superstructure.

Additional insights regarding the nature of the two frictional mechanisms can be obtained by plotting lateral force trace loops (corresponding to the maps appearing in Figure 3b-c) measured in the two velocity regimes. Figure 3d presents a friction force trace loop measured at a sliding velocity of $4.1 \, \text{nm/s}$ demonstrating three characteristic features: (i) atomic scale lateral force undulations with periodicity of the hexagonal graphene lattice along the sliding direction; (ii) smooth larger-scale modulations with a period corresponding to that of the moiré superlattice; and (iii) minor hysteresis between the lateral force trace and retrace, indicative of negligible energy dissipation. Figure 3e presents the corresponding lateral force trace loop measured at a sliding velocity of $390.6 \, \text{nm/s}$ - above the threshold velocity. Here, a qualitatively different behavior is found, where the atomic scale features prevail, whereas the larger-scale modulations turn into clear dissipative stick-slip motion with notable hysteresis in the friction loop.
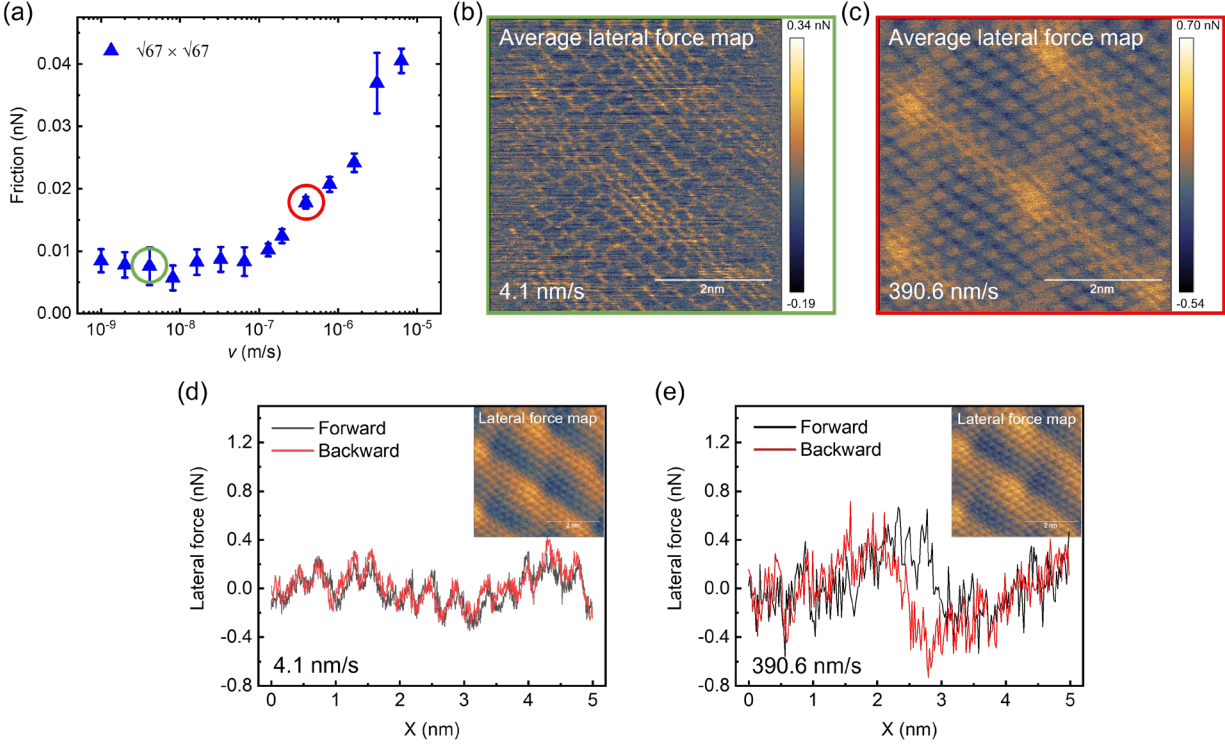
Figure 3. Emergence of dissipative moiré stick-slip motion. (a) Dependence of the measured friction force on the tip sliding velocity for the $\sqrt{67} \times \sqrt{67}$ moiré superstructure. (b)-(c) Average lateral force maps measured at $4.1\ nm/s$ and $390.6\ nm/s$, respectively. (d)-(e) Forward (black) and backward (red) lateral force traces corresponding to the maps presented in panels (b) and (c), respectively, at the two sliding velocities (the insets show the corresponding forward lateral force maps).

The transition of the frictional velocity dependence from nearly constant ultralow values ($\lesssim 10$ pN) at lower speeds to logarithmic scaling at higher speeds, was observed also for the 2×2 and 4×4 moiré superstructures considered (see Figure 4a). Importantly, within the sensitivity of our experimental setup, the measured low-speed regime friction forces are practically the same for all cases studied. This indicates that the low-speed friction is unaffected by the presence of moiré superstructures, in line with our finding that at low tip sliding velocities the moiré-scale lateral force traces feature smooth modulations rather than dissipative stick-slip motion. Notably, the threshold velocity for the emergence of logarithmic friction scaling does depend on the character of the superstructure, where the transition shifts to lower velocity values with increasing moiré periodicity. Furthermore, in the high sliding velocity regime, the friction force is larger for moiré superstructures of higher periodicity at any given velocity.

The threshold velocity separating the two frictional regimes depends also on the normal load applied to the AFM cantilever. Figure 4b shows the velocity dependence of the measured friction for the $\sqrt{67} \times \sqrt{67}$ moiré superstructure under normal loads of 1, 5 and 10 nN, demonstrating that the threshold velocity decreases with increasing normal load. At the low velocity regime, the friction forces are practically independent of the normal load as expected for superlubric sliding. Conversely, above the threshold velocity, friction grows significantly with increasing normal load (in agreement with recent experimental observations[34]), suggesting the breakdown of superlubricity.
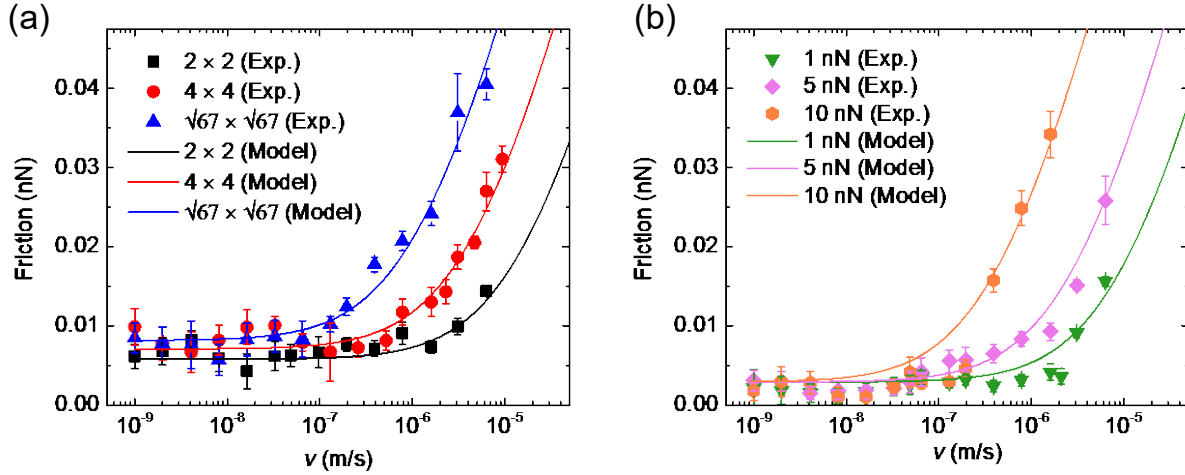

Figure 4. Effects of moiré superlattice dimensions (a) and external normal load (b) on the velocity dependence of the kinetic friction force. In panel (a) moiré supercell periodicities of 0.5 (black squares), 1 (red circles), and 2.2 (blue triangles) nm are considered with a normal load of 2 nN. In panel (b) normal loads of 1 (green triangles), 5 (magenta diamonds), and 10 (orange hexagons) nN are considered for the $\sqrt{67} \times \sqrt{67}$ moiré superstructure. The difference in the nearly constant friction measured at low velocities in panels (a) and (b) is attributed to the two different AFM tips used in the corresponding measurements in each panel. The solid lines are model fittings based on Eq. (6) with the following fitting parameters - in panel (a): $x_0 = 1$ Å, $T = 300$ K, $\kappa = 0.4$ N/m and $\Delta E_{ad} = 0.04 \, k_B T$ and $k_d^0 = 1.5 \times 10^5$ Hz for the black line, $\Delta E_{ad} = 0.06 \, k_B T$ and $k_d^0 = 4 \times 10^4$ Hz for the red line and $\Delta E_{ad} = 0.08 \, k_B T$ and $k_d^0 = 1 \times 10^4$ Hz for the blue line; in panel (b): $x_0 = 1$ Å, $T = 300$ K, $\kappa = 0.2$ N/m, $\Delta E_{ad} = 0.02 \, k_B T$ and $k_d^0 = 4 \times 10^4$ Hz for the green line, $k_d^0 = 1.2 \times 10^4$ Hz for the magenta line, and $k_d^0 = 1.8 \times 10^3$ Hz for the orange line.

The nature of the new moiré-scale frictional mechanism discovered could, in principle, be rationalized via fully atomistic molecular dynamic (MD) simulations of the sliding interface. Unfortunately, due to computational limitations, such simulations are currently restricted to either extremely high velocities (~4-8 orders of magnitude higher than the experimental conditions) or to the zero-velocity limit (quasi-static simulations). Hence, we cannot use such simulations to capture the transition between superlubric sliding at low-velocities and dissipative sliding with logarithmic scaling of friction at intermediate velocities, directly. Nevertheless, we can definitely use MD simulations to explore the friction dependence on normal load and moiré supercell dimensions. This, in turn, provides key information that can be harnessed to construct phenomenological models that, in turn, can be used to explore the velocity dependence of friction at the experimentally relevant velocity range, giving insights regarding the transition mechanism. Below we follow this approach to bridge the gap between MD simulations and experiments.

Our MD simulation setup consists of a hemispherical diamond tip model of radius ~ 2.5 nm sliding over graphene moiré superstructures atop a Pt(111) surface. To study the effect moiré superstructure dimensions on friction, the graphene was rotated to generate moiré superstructures with different periods of ~2.2, ~1.0, and ~0.4 nm, comparable to the experimental configurations. Dynamic simulations were performed using the LAMMPS package[35] with a sliding velocity of 2 m/s, at zero temperature, and under normal loads ranging from 0 to 24 nN (see SI section 4 for further simulation details).

Figure 5a, b present the averaged in-plane displacement along the sliding direction (a) and out of plane displacement (b) of two covalently bonded atoms located at the top of one of the ridges (see Figure 5c) of a 2.2 nm periodic moiré superstructure, during tip sliding under three different normal loads. At zero normal load, we observe smooth in-plane variations of the atomic position during sliding with a relatively small amplitude (0.2 Å). These are accompanied by minor depression of the ridge upon tip crossing. We note that while maximal in-plane displacement occurs at sliding distances of 0.9 and 3.1 nm the out-of-plane depression occurs only at a sliding distance of 3.1 nm. The reason for not observing depression at a sliding distance of 0.9 nm is that we measure the height of atoms located on ridge 2, while the tip at this point crosses ridge 1. On the contrary, when the tip crosses one ridge the superstructure exhibits non-local in-plane displacements (see supplementary movies 1-2). Upon increasing normal load, the smooth in-plane displacement turns

8

into clear dissipative stick-slip motion accompanied by increased ridge depression. The underlying mechanism relates to the fact that when the tip approaches a moiré ridge, it pushes the ridge forward. Upon further tip motion the in-plane stretching of the graphene surface overcomes the tip-ridge interaction energy causing the ridge to detach from the tip and abruptly retract towards its equilibrium position (see Figure 1b-c). These surface deformations are manifested in the calculated lateral force traces, which serve as our experimental observables. Figure 5d presents the lateral force traces calculated under three normal loads. In agreement with our experimental findings, regardless of the normal load, two periodicities are observed in the force traces, the smaller period corresponding to atomic features, whereas the larger period matches the period of the moiré superstructure. At low normal loads, the lateral force trace exhibits smooth oscillations at both scales leading to a negligible average force, which is indicative of ultra-low friction. Increasing the normal load, saw-tooth like behavior of the lateral force trace develops on both scales, resulting in dissipative stick-slip motion. In Figure 5e we compare results of similar simulations performed for twisted moiré superstructures of different dimensions under a normal load of 12.3 nN. Naturally, the atomic features appear in all cases with a slightly modified periodicity due to the different orientation of the hexagonal lattice with respect to the tip sliding direction. Moiré-scale friction, however, becomes visible only when the moiré superstructures dimensions are significantly larger than the atomic lattice, allowing for a corrugated moiré lattice to develop.

9
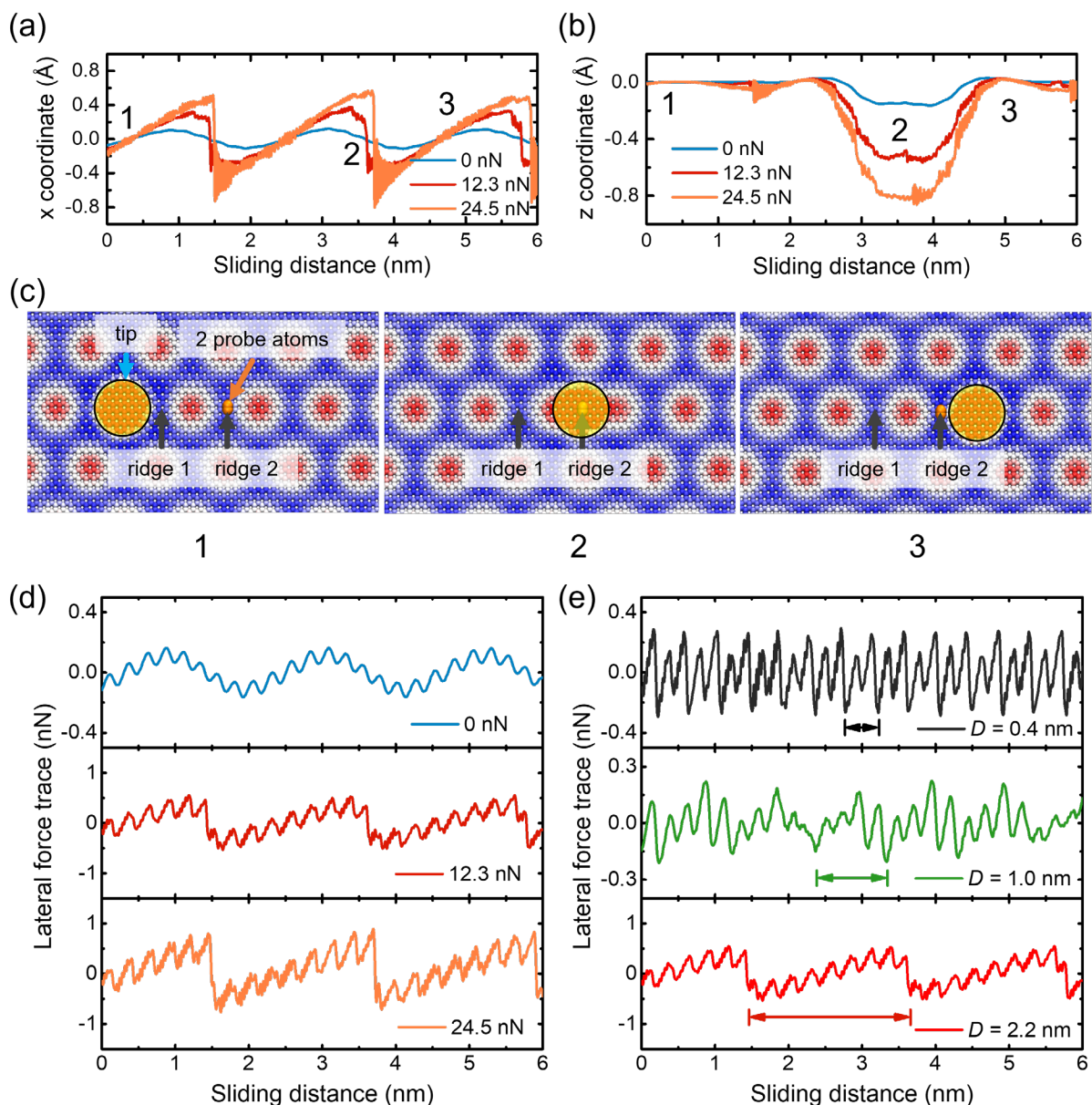
Figure 5. MD simulation results. (a) in-plane displacement along the tip sliding direction and (b) out-of-plane displacement of atoms located at moiré ridge 2 under normal loads of zero (blue), 12.3 (red), and 24.5 (orange) nN. (c) Snapshots corresponding to the sliding distances marked in panels (a) and (b), showing the relative positions of the tip and the probe atoms at the moiré ridge 2. (d) Lateral force traces corresponding to the simulation results presented in panels (a) and (b). (e) Lateral force traces calculated under a normal load of 12.3 nN for moiré supercell dimensions of 0.4 nm (black upper panel), 1.0 nm (green, middle panel), and 2.2 nm (red, lower panel). The arrows in panel (e) correspond to the moiré supercell period, which aligns with the sliding direction. For clarity, the trajectories and force trances are smoothened using the Savitzky-Golay method.

10

Both our experiments and the MD simulations demonstrate that the atomic contribution to friction in our system is negligible and the main energy dissipation route involves moiré-scale stick-slip dynamics due to tip-ridge interactions. Based on this understanding, we derive a phenomenological model that spans velocity and load regimes relevant to the experimental conditions. Following the spirit of models developed to describe pulling induced unbinding of molecular bonds in single molecule force spectroscopy experiments[36], our two-state model considers the sliding tip attachment to-, pushing of-, and detachment from a moiré ridge. The probability to find the tip attached to the ridge, $p_a(t)$, is described by the following master equation:

$$\frac{dp_a(t)}{dt} = -k_d(t)p_a + k_a(t)p_d,$$ (1)

where $p_d(t)$ is the probability to find the tip detached from the ridge, and $k_d(t)$ and $k_a(t)$ are the instantaneous detachment and attachment rates, respectively, which depend on the applied force. The detachment and attachment rates are approximated using the Bell model,[37] where the corresponding barriers are calculated considering the combined effect of the potentials experienced by the tip due to its interaction with the ridge and with the moving stage. The former is represented by a two-state potential landscape, whereas the latter is described by a harmonic spring of effective force constant κ and zero equilibrium length (see SI section 5 for an explicit derivation). The resulting expression for the detachment rate is:

$$k_d(F) = k_d^0 \exp\left[\beta\left(Fx_0 - \frac{1}{2}\kappa x_0^2\right)\right],$$ (2)

where k_d^0 is the detachment rate in the absence of the external spring, $\beta = (k_B T)^{-1}$, k_B is Boltzmann's constant, T is the temperature, F is the force experienced by the tip due to the moving stage, x_0 is the distance between the minimum corresponding to the attached state and the transition barrier along the tip-ridge interaction potential profile. Similarly, the attachment rate is given by:

$$k_a(F) = k_a^0 \exp\left[-\frac{\beta\kappa}{2}\left(\frac{F}{\kappa} - x_0\right)^2\right] = k_d(F) \exp\left[\beta\left(\Delta E_{ad} - \frac{F^2}{2\kappa}\right)\right],$$ (3)

where k_a^0 is the attachment rate in the absence of the external spring, and $\Delta E_{ad} = E_d - E_a$ is the energy difference between the attached and detached states obeying the relation $e^{\beta\Delta E_{ad}} = k_a^0/k_d^0$. From Eq. 3 we see that the attachment and detachment rates (as well as the corresponding barriers) become equal when the applied force, often termed the equilibrium force, is:

11

$$F_{eq} = \sqrt{2\kappa\Delta E_{ad}}. \tag{4}$$

Below F_{eq} the attachment rate is dominant, essentially keeping the tip attached to the ridge, whereas above F_{eq} the detachment rate becomes dominant and the tip is mostly in the detached state. Substituting Eq. (2) into Eq. (1) and integrating Eq. (1) from F_{eq}, the ensemble averaged detachment force can be obtained as:

$$\langle F \rangle_d(v) = F_{eq} + F_\beta e^{\frac{v^*}{v}} E_1\left(\frac{v^*}{v}\right), \tag{5}$$

where $F_\beta \equiv k_B T/x_0$ is a characteristic thermal force, $E_1(x) = \int_x^\infty \frac{e^{-x}}{x} dx$ is the exponential integral, $v^* \equiv k_d(F_{eq}) F_\beta/\kappa$, and v is the stage velocity. The kinetic friction force can then be evaluated from the area enclosed during a single stick-slip cycle divided by the corresponding tip displacement. Assuming that the lateral force increases linearly with stage displacement during the stick stage, and that the force drops approximately to zero after detachment (see SI Fig. S7), the triangular lateral force trace yields a kinetic friction force of

$$\langle F \rangle_k(v) = \frac{1}{2}\langle F \rangle_d(v). \tag{6}$$

Examining the velocity dependence of the kinetic friction force experienced by the tip given by Eq. (6) at the low and high velocity regimes reveals qualitatively different characteristics. At the low velocity limit ($v \ll v^*$), the asymptotic expansion[38] $E_1(x) \sim \frac{\exp(-x)}{x}\left(1 - \frac{1}{x} + \cdots\right)$ for $x \gg 1$ can be used to obtain $\langle F \rangle_k(v) \sim \frac{1}{2}F_{eq} + \frac{1}{2}F_\beta v/v^*$. The weak velocity dependence of the force in this regime in our experiments, suggests that $F_\beta/v^* \ll v$ in our case. At the high velocity regime, one can use the small-x expansion $E_1(x) = -\gamma - \ln(x) + x - \frac{x^2}{8} + \cdots$,[38] where $\gamma \cong 0.577$ is the Euler's constant, to yield $\langle F \rangle_k(v) \approx \frac{1}{2}F_\beta\left[\ln\left(\frac{v}{v^*}\right) - \gamma\right]$, showing a logarithmic scaling of the friction with velocity, in agreement with our experimental findings.

To fit the results of this model to the experimental observations we note that increasing the moiré ridge height (via, e.g., controlling the twist angle and changing the superlattice dimensions) or increasing the external normal load leads to enhanced lead-tip interactions. We can therefore approximate the detachment barrier height to depend linearly on the superlattice dimensions and the external normal load. Accordingly, in the spirit of the Arrhenius rate constant law, the

detachment rate, k_d^0, exponentially decreases with increasing moiré size and normal load. These assumptions are supported by our atomistic simulation results presented in Figure 5d demonstrating the emergence of moiré-scale stick-slip motion with increasing supercell dimensions, and Figure 5a, b, where the lateral and normal deformations are found to grow with normal load. For simplicity, we also assume that the effective spring constant, κ, and the detachment barrier position, x_0, are independent of the moiré supercell dimensions and external normal load. The fitting results, presented as the colored solid curves in Figure 4, are in remarkable agreement with the experimental results, capturing the velocity dependence of friction for different moiré supercell dimensions and normal loads. Notably, not only are the two velocity regimes well captured, but also the dependence of the threshold velocity on both moiré supercell dimensions and on the applied normal load is well described.

We note that a similar logarithmic friction dependence on velocity at the high velocity regime was predicted by Prandtl-Tomlinson and multi-contact models.[5,39-43] However, unlike the latter, which predict linear decrease of friction (down to zero) with velocity reduction at the low velocity regime, our phenomenological model is able to capture the velocity leveling obtained in our experiments. This can be rationalized by the fact that if the detachment force would reduce below F_{eq}, the barrier for tip attachment to the ridge would be considerably smaller than the corresponding detachment barrier and the tip will immediately reattach after each detachment event. Hence, the friction force, as well, will reach a plateau.

The phenomenological model thus bridges the gap between experiment and atomistic simulations. This allows us to decipher the mechanisms underlying velocity dependence of the friction force experienced by a tip sliding over complex moiré superstructures formed at incommensurate interfaces involving layered materials. In these systems, atop the well-known atomic stick-slip motion features, and possible puckering effects,[44] dissipative moiré-scale stick-slip characteristics emerge in the friction force traces. Similar to atomic-scale friction, moiré-scale dynamics exhibits logarithmic scaling of friction with velocity, at the high velocity regime, where, according to our atomistic simulations, the main energy dissipation route involves moiré ridge elastic deformation and strain relaxation upon tip sliding. Conversely, at low velocities, the moiré-scale friction force levels off to a finite value, associated with the equilibrium detachment force. Using the phenomenological model, we find that the threshold velocity separating these two regimes is

proportional to the tip-ridge detachment rate, which explains its experimentally observed dependence on moiré supercell dimension and applied normal load. Naturally, double-periodic friction over moiré superlattices is not limited to the case of graphene on Pt(111) surfaces. Hence, we expect that the revealed mechanism for moiré-scale friction dependence on velocity will emerge in other interfaces, such as graphene/*h*-BN[20,29,30] or graphene/Ru(0001)[28] heterostructures, where variations in the graphene/substrate interactions may lead to further interesting tribological characteristics.

References:

1 Vanossi, A., Manini, N., Urbakh, M., Zapperi, S. & Tosatti, E. Colloquium: Modeling friction: From nanoscale to mesoscale. *Rev. Mod. Phys.* **85**, 529-552, (2013).

2 Hod, O., Meyer, E., Zheng, Q. & Urbakh, M. Structural superlubricity and ultralow friction across the length scales. *Nature* **563**, 485-492, (2018).

3 Sang, Y., Dubé, M. & Grant, M. Thermal Effects on Atomic Friction. *Phys. Rev. Lett.* **87**, 174301, (2001).

4 Dudko, O. K., Filippov, A. E., Klafter, J. & Urbakh, M. Dynamic force spectroscopy: a Fokker–Planck approach. *Chem. Phys. Lett.* **352**, 499-504, (2002).

5 Gnecco, E. *et al.* Velocity Dependence of Atomic Friction. *Phys. Rev. Lett.* **84**, 1172-1175, (2000).

6 Li, Q., Dong, Y., Perez, D., Martini, A. & Carpick, R. W. Speed Dependence of Atomic Stick-Slip Friction in Optimally Matched Experiments and Molecular Dynamics Simulations. *Phys. Rev. Lett.* **106**, 126101, (2011).

7 Riedo, E., Gnecco, E., Bennewitz, R., Meyer, E. & Brune, H. Interaction Potential and Hopping Dynamics Governing Sliding Friction. *Phys. Rev. Lett.* **91**, 084502, (2003).

8 Sharp, T. A., Pastewka, L. & Robbins, M. O. Elasticity limits structural superlubricity in large contacts. *Phys. Rev. B* **93**, 121402, (2016).

9 Sharp, T. A., Pastewka, L., Lignères, V. L. & Robbins, M. O. Scale- and load-dependent friction in commensurate sphere-on-flat contacts. *Phys. Rev. B* **96**, 155436, (2017).

10 Dietzel, D., Brndiar, J., Štich, I. & Schirmeisen, A. Limitations of Structural Superlubricity: Chemical Bonds versus Contact Size. *ACS Nano* **11**, 7642-7647, (2017).

11 Gao, X., Ouyang, W., Hod, O. & Urbakh, M. Mechanisms of frictional energy dissipation at graphene grain boundaries. *Phys. Rev. B* **103**, 045418, (2021).

12 Gao, X., Ouyang, W., Urbakh, M. & Hod, O. Superlubric polycrystalline graphene interfaces. *Nat. Commun.* **12**, 5694, (2021).

13 Mandelli, D., Leven, I., Hod, O. & Urbakh, M. Sliding friction of graphene/hexagonal–boron nitride heterojunctions: a route to robust superlubricity. *Sci. Rep.* **7**, 10851, (2017).

14 Woods, C. R. *et al.* Commensurate–Incommensurate Transition in Graphene on Hexagonal Boron Nitride. *Nat. Phys.* **10**, 451, (2014).

15 Dienwiebel, M. *et al.* Superlubricity of graphite. *Phys. Rev. Lett.* **92**, 126101, (2004).

16 Filleter, T. *et al.* Friction and Dissipation in Epitaxial Graphene Films. *Phys. Rev. Lett.* **102**, 086102, (2009).

17 Song, Y. *et al.* Robust microscale superlubricity in graphite/hexagonal boron nitride layered heterojunctions. *Nat. Mater.* **17**, 894, (2018).

18 Liao, M. *et al.* UItra-low friction and edge-pinning effect in large-lattice-mismatch van der Waals heterostructures. *Nat. Mater.*, (2021).

19 Berman, D., Erdemir, A. & Sumant, A. V. Approaches for Achieving Superlubricity in Two-Dimensional Materials. *ACS Nano* **12**, 2122-2137, (2018).

20 Leven, I., Krepel, D., Shemesh, O. & Hod, O. Robust Superlubricity in Graphene/h-BN Heterojunctions. *J. Phys. Chem. Lett.* **4**, 115-120, (2013).

21 Zhang, Z. *et al.* Macroscale Superlubricity Enabled by Graphene-Coated Surfaces. *Adv. Sci.* **7**, 1903239, (2020).

22 Berman, D., Deshmukh, S. A., Sankaranarayanan, S. K. R. S., Erdemir, A. & Sumant, A. V. Macroscale superlubricity enabled by graphene nanoscroll formation. *Science* **348**, 1118-1122, (2015).

23 Liu, S.-W. *et al.* Robust microscale superlubricity under high contact pressure enabled by graphene-coated microsphere. *Nat. Commun.* **8**, 14029, (2017).

24 Mandelli, D., Ouyang, W., Urbakh, M. & Hod, O. The Princess and the Nanoscale Pea: Long-Range Penetration of Surface Distortions into Layered Materials Stacks. *ACS Nano* **13**, 7603-7609, (2019).

25 Chan, N. *et al.* Contrast in nanoscale friction between rotational domains of graphene on Pt(111). *Carbon* **113**, 132-138, (2017).

26 Zheng, X. *et al.* Robust ultra-low-friction state of graphene via moiré superlattice confinement. *Nat. Commun.* **7**, 13204, (2016).

27 Filleter, T. & Bennewitz, R. Structural and frictional properties of graphene films on SiC(0001) studied by atomic force microscopy. *Phys. Rev. B* **81**, 155412, (2010).

28 Shi, R. *et al.* Moiré superlattice-level stick-slip instability originated from geometrically corrugated graphene on a strongly interacting substrate. *2D Mater.* **4**, 025079, (2017).

29 Zhang, S. *et al.* Dual-Scale Stick-Slip Friction on Graphene/$h-$BN Moiré Superlattice Structure. *Phys. Rev. Lett.* **128**, 226101, (2022).

30 Huang, K. *et al.* The Origin of Moiré-Level Stick-Slip Behavior on Graphene/h-BN Heterostructures. *Adv. Funct. Mater.* **n/a**, 2204209, (2022).

31 Mandelli, D., Ouyang, W., Hod, O. & Urbakh, M. Negative Friction Coefficients in Superlubric Graphite--Hexagonal Boron Nitride Heterojunctions. *Phys. Rev. Lett.* **122**, 076102, (2019).

32 Gao, X., Urbakh, M. & Hod, O. Moiré Superstructure Stick-Slip Dynamics in Polycrystalline 2D Material Interfaces. *under review*, (2022).

33 Gao, M. *et al.* Epitaxial growth and structural property of graphene on Pt(111). *Appl. Phys. Lett.* **98**, 033101, (2011).

34 Liu, Z. *et al.* Dissipation mechanism of two-dimensional materials: Slip of moiré tiles. *under review*, (2022).

35 Plimpton, S. Fast Parallel Algorithms for Short-Range Molecular Dynamics. *J. Comput. Phys.* **117**, 1-19, (1995).

36 Friddle Raymond, W., Noy, A. & De Yoreo James, J. Interpreting the widespread nonlinear force spectra of intermolecular bonds. *Proc. Natl. Acad. Sci. U.S.A.* **109**, 13573-13578, (2012).

37 Bell George, I. Models for the Specific Adhesion of Cells to Cells. *Science* **200**, 618-627, (1978).

38 Barry, D. A., Parlange, J. Y. & Li, L. Approximation for the exponential integral (Theis well function). *J. Hydrol.* **227**, 287-291, (2000).

39 Barel, I., Urbakh, M., Jansen, L. & Schirmeisen, A. Multibond Dynamics of Nanoscale Friction: The Role of Temperature. *Phys. Rev. Lett.* **104**, 066104, (2010).

40 Ouyang, W., Cheng, Y., Ma, M. & Urbakh, M. Load-velocity-temperature relationship in frictional response of microscopic contacts. *J. Mech. Phys. Solids* **137**, 103880, (2020).

41 Prandtl, L. Ein Gedankenmodell zur kinetischen Theorie der festen Körper. *Z. Angew. Math. Mech.* **8**, 85-106, (1928).

42 Tomlinson, G. A. CVI. A molecular theory of friction. *Philos. Mag.* **7**, 905-939, (1929).

43 Jinesh, K. B., Krylov, S. Y., Valk, H., Dienwiebel, M. & Frenken, J. W. M. Thermolubricity in atomic-scale friction. *Phys. Rev. B* **78**, 155440, (2008).

44 Lee, C. *et al.* Frictional Characteristics of Atomically Thin Sheets. *Science* **328**, 76-80, (2010).